Cancer Nanotechnology

RESEARCH Open Access

Engineering M1-derived nanovesicles loading with docosahexaenoic acid synergizes ferroptosis and immune activation for treating hepatocellular carcinoma

Ming Meng[1†], Xia Zhang[2†], Qian Li[3], Jingjing Han[3], Yu Chen[3], Haishi Qiao[4], Yonglin Yang[2*] and Xin Huang[4*]

†Ming Meng and Xia Zhang These authors contributed equally to this work

*Correspondence: easing@163.com; cpuhuangxin@cpu.edu.cn

[1] Department of Neurology, Taizhou Third Peoples Hospital, Taizhou, Jiangsu, China
[2] Department of Infectious Diseases, The Affiliated Taizhou Peoples Hospital of Nanjing Medical University Taizhou School of Clinical Medicine Nanjing Medical University, Taizhou, Jiangsu, China
[3] Department of Anesthesiology, The First Affiliated Hospital of Nanjing Medical University, Nanjing, Jiangsu, China
[4] Department of Pharmaceutical Engineering, School of Engineering, China Pharmaceutical University, Nanjing, China

Abstract

Ferroptosis represents an innovative strategy to overcome the resistance of traditional cancer therapeutic through lethal lipid peroxidation leading to immunogenic cell death. However, the inefficiency of ferroptosis inducers and mild immunogenicity restrict the further clinical applications. Herein, engineering exosome-mimic M1 nanovesicles (MNV) were prepared by serial extrusion of M1 macrophage and served as an efficient vehicle for docosahexaenoic acid (DHA) delivery. MNV loaded with DHA (MNV@DHA) could promote more DHA accumulation in tumor cells, depletion glutathione and reduction of lipid antioxidant glutathione peroxidase-4 facilitating the occurrence of ferroptosis. Furthermore, MNV were able to induce the polarization of M1 and repolarize M2 macrophages to activate tumor immune microenvironments. The activated immune cells would further trigger the ferroptosis of tumor cells. In a murine orthotopic hepatocellular carcinoma model, MNV@DHA could significantly target tumor tissues, increase the proportion of M1 macrophages and $CD8^+$ T cells and lessen the infiltration of M2 macrophages. Accordingly, MNV@DHA characterized with positive feedback regulation between ferroptosis and immune activation exhibited the strongest in vivo therapeutic effect. The synergism of ferroptosis and immunomodulation based on the dietary polyunsaturated fatty acids and engineered exosome-mimic nanovesicles may serve as a promising modality to efficiently complement pharmacological approaches for cancer management.

Keywords: Docosahexaenoic acid, Ferroptosis, Exosome-mimic, Drug delivery, Immunotherapy

Introduction

Ferroptosis has been increasingly considered as a novel type of programmed cell death that can overcome drug-resistance of cancer cells upon conventional apoptosis-based cancer interference (Chen et al. 2021; Conrad et al. 2019; Kim et al. 2022). The vital step of ferroptosis is the Fenton reaction characteristically initiated between ferric ions and intratumoral hydrogen peroxide to generate reactive oxygen species (ROS). The ROS

induce lethal lipid peroxidation that will cause rupture of cell membrane resulting in cell death (Yang et al. 2014). During this process, mild immune activation might be occurred contributing from damage-associated molecular patterns (DAMPs) such as HMGB1 protein released from ferroptosis cells to activate macrophages (Jiang et al. 2020; Shen et al. 2018). Therefore, the ferroptosis pattern could be employed to combine with immunotherapy for tumor management (Liao et al. 2022). However, the limited tumor targeting capacity, inadequate therapeutic efficiency of ferroptosis-inducers, and tumor immunosuppressive microenvironments (TIME) have seriously restricted the further application of ferroptosis-based cancer treatment in vivo (Li P. et al. 2021a; Zhang et al. 2020). Therefore, optimizing the delivery strategies for ferroptosis agents and reprogramming TIME are promising in cancer management.

Tumor associated macrophages (TAMs) play an important role in the development of TIME (Mantovani et al. 2017). It is broadly considered that TAMs can be divided into two subtypes of antitumoral M1-type and protumoral M2-type (Zhao et al. 2022). M2 macrophages play a dominant role in development of TIME, promoting immune escape of tumor cells and lessening the infiltration of antitumoral lymphocytes (Li et al. 2019). Repolarizing M2 macrophage into M1-type represents a promising strategy to activate TIME for antitumor treatment (Shan et al. 2020). Although several therapeutic agents including related antibody, siRNA and small molecules have be explored for M2 repolarization in preclinical studies (Colegio et al. 2014; Rodell et al. 2018), the hurdles including non-preferential transport, low efficiency of polarization and sub-optimal therapeutic effect restrict the broad application in clinical treatments (Li P. et al. 2021b). DAMPs have been demonstrated to serve as one of the feasible means to promote the polarization of M1 macrophages (Komai et al. 2017; Luo et al. 2021). Furthermore, M1 macrophages had been reported to promote tumor ferroptosis by enhancing tumor vulnerability to oxidative damage and activating a tumor-eradicating immune response within the TIME (Chen et al. 2021; Pan et al. 2020; Zhou et al. 2022). M1 could directly release peroxides for the promotion of tumor ferroptosis through accelerating the intracellular Fenton reaction (Haschka et al. 2021). Another mechanism had been demonstrated that activated M1 could initiate $CD8^+$ cytotoxic T lymphocytes to release interferon-γ (IFN-γ), which could downregulate the expression of SLC3A2 and SLC7A11 in tumor cells triggering ferroptosis (Liao et al. 2022; Wang et al. 2019). Thus, combining the polarization of M1 macrophages with a ferroptosis inducer might exhibit a synergistic antitumor effect via positive feedback of immune activation in TIME.

A series of studies have reported that exosomes derived from M1 macrophages could induce polarization of M1 from M0 macrophages and reprogram protumoral M2 to antitumoral M1-type (Cheng et al. 2017; Nie et al. 2020). However, the natural exosomes have some disadvantages including unavailability in large quantity, limited modifiability and low efficiency of drug loading, which seriously hinder the progress of exosome in clinical application (Choo et al. 2018; Jang et al. 2013). Recent studies revealed an innovative strategy to produce exosome mimics via extruding whole cells into exosome-scale nanovesicles, which were endowed with paralleled characteristic compared to natural exosomes (Molinaro et al. 2016; Yang et al. 2016). The nanovesicles extruded from M1 macrophages would inherit the proinflammatory factors, ligands and receptors expressed on cell membrane, which were benefited to the polarization of M1

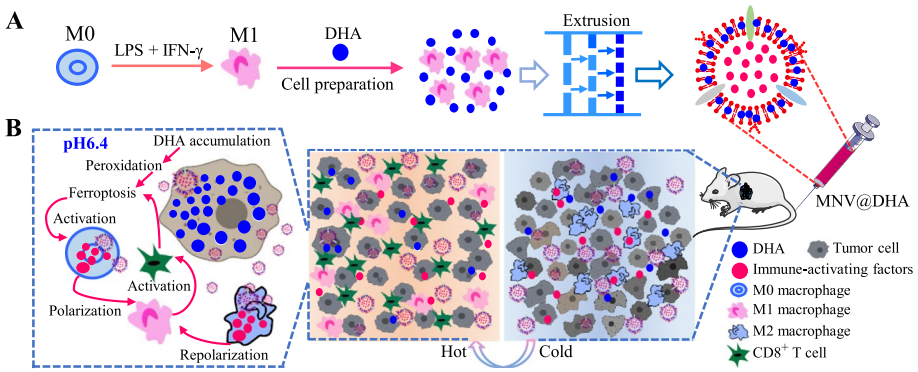

Scheme 1. Schematic diagram illustration of MNV@DHA for orthotopic hepatocellular carcinoma treatments. **A** The prepared process of MNV@DHA. **B** The in vivo antitumor effect of MNV@DHA based on positive-feedback induction of ferroptosis and immune activation

macrophages (Choo et al. 2018; Li Q. et al.(2021c)). More importantly, the preparation methods might meet the request of industrialization, thereby increasing the potential for the clinical development of nanovesicles-based drug delivery system.

The nanovesicles of exosome-mimic from M1 macrophages could be utilized to load ferroptosis inducers against cancer based on positive-feedback of ferroptosis and immune activation. Polyunsaturated fatty acid including docosahexaenoic acid (DHA) had been reported to induce ferroptosis (Kepp et al. 2022; Zhang et al. 2022). Liao et al. reported that T cell-derived IFN-γ in combination with arachidonic acid induced immunogenic tumor ferroptosis, serving as a mode of action for $CD8^+$ T cell-mediated tumor killing (Liao et al. 2022). Furthermore, Dierge et al. demonstrated the acidic tumor environment could promote the accumulation of DHA and induce ferroptosis in cancer cells under ambient acidosis (Dierge et al. 2021). In hepatocellular carcinoma cells (HCC), DHA had been reported to be reconstituted with low-density lipoprotein for the induction of ferroptosis (Ou et al. 2017). Herein, the nanovesicles (MNV) extruded from M1 macrophages were loaded with DHA to cooperatively fight against HCC (Scheme 1). MNV loaded with DHA (MNV@DHA) could significantly increase the DHA accumulation in HCC cells, which was advantaged to the induction of ferroptosis and immune activation. Furthermore, MNV can promote the polarization of M1 macrophage, repolarize M2 to M1-type, and reprogram the TIME, contributing to the further amplification of tumor cell ferroptosis. In vivo experiments demonstrated that MNV@DHA could target murine orthotopic HCC, induce ferroptosis of tumor cells and activate TIME exhibiting significant antitumor activity. Thus, this easily prepared nanovesicles loaded with dietary omega-3 polyunsaturated fatty acids possess enormous potential for the clinical tumor treatment and may efficiently complement current pharmacological approaches.

Materials and methods

Materials and reagents

Docosahexaenoic Acid (DHA) was purchased from Shanxi Xiazhou Biotechnology Co., Ltd. (Shanxi, China). Ferrostatin-1 was obtained from Selleck Chemicals. Murine IFN-γ was obtained from Sino Biological. Lipopolysaccharide (LPS), Propidium iodide (PI),

ROS probe, GSH detection kit, Oil Red, and hematoxylin were purchased from Beyotime Biotechnology. (Nantong, China). DiR was purchased from Yeasen Biotechnology Co., Ltd. (Shanghai, China). The fluorescence-labelled antibody CD86 and CD 206 for flow cytometry analysis was purchased from BioLegend. The antibody of GPX4 and GAPDH for blot assay was obtained from Abcam. SLC7A11 was purchased from Proteintech (Wuhan, China). The Raw 264.7 cells were purchased from the Shanghai Cell Bank (Shanghai, China). The H22-Luc cells were obtained from Procell (Wuhan, China). Cells were cultured in Roswell Park Memorial Institute 1640 (RPMI 1640) with high glucose or Dulbecco's modified eagle's medium (DMEM) with high glucose, supplemented with 10% heat inactivated fetal bovine serum (FBS), 2 mM glutamine, nonessential amino acids, and sodium pyruvate. The medium and supplements were purchased from Thermo Fisher Scientific. Cells were cultured at 37 C in a humidified chamber with 5% CO_2.

Characterization of nanovesicles

Dynamic light scattering (DLS, Anton Paar Litesizer 500) and transmission electron microscopy (TEM, FEI Philips Tecnai 20) were utilized to determine the size and morphology of the nanovesicles, respectively. The DLS was utilized to determine the Zeta potential of nanovesicles. Fluorescence images for cellular uptake, ROS detection, CD86 and CD206 expression was performed by a fluorescence microscope (IX73, Olympus, Japan). Fluorescence analysis was performed using a flow cytometer (Beckman CytoFLEX, USA). In vivo imaging was performed using a near-infrared fluorescence imaging system (IVIS® Lumina™, USA).

MNV@DHA Preparation

The MNV was obtained from M1 macrophages by extrusion. Briefly, RAW 264.7 cells were stimulated with LPS (100 ng/mL) and IFN-γ (50 ng/mL) for 24 h and then CD86 expression was examined using a flow cytometer to confirm the polarization of M1 macrophages. After the successful polarization of M1 macrophages, cells were washed twice with PBS. Then, the prepared M1 macrophages and DHA were mixed and sequentially extruded through polycarbonate membrane filters with pore sizes of 1 μm, 0.4 μm and 0.2 μm for 21 times using a mini-extruder (Avanti Polar Lipids) to obtain nanosized extracellular vesicles. The unbroken cells or cell debris were separated by centrifugation (400 ×g) for 5 min and the supernatant was collected and performed with dialysis to remove free DHA. The MNV@DHA were then ultracentrifuged (100,000 ×g) for 2 h at 4 °C in a density gradient containing 50% of iodixanol (1 mL), 10% of iodixanol (2 mL) and the sample (7 ml) from bottom to top. The purified MNV@DHA were obtained from the interface of the 50% and 10% iodixanol layers followed by three times of PBS rinsing. The protein content of the exosome-mimetic MNV@DHA was determined using a BCA protein assay kit and then stored at 4 °C for characterization analysis.

Stability analysis

The stability of MNV@DHA was evaluated by monitoring the size change of nanovesicles dispersed in PBS and 10% of FBS, respectively. Briefly, the prepared MNV@DHA

(10 μg/mL) was dispersed in PBS and 10% of FBS and then stored at 4 °C. The size of nanovesicles was determined at different time intervals by DLS.

Coomassie blue staining assay

Sodium dodecyl-sulfate polyacrylamide gel electrophoresis (SDS-PAGE) was used to separate protein samples of M0, M1 macrophages, MNV and MNV@DHA. Briefly, the nanovesicles were prepared as described above and then resuspended in 100 μL of PBS followed by the addition of 50 μL loading buffer and then denatured by incubation at 95 °C for 15 min. Finally, the protein sample were separated by 8% of SDS-PAGE followed by Coomassie blue staining.

Accumulative drug release

The drug loading efficiency and accumulative release of DHA from MNV at different pH conditions (pH 7.4 and 5.0) was determined by high performance liquid chromatography (HPLC). Briefly, two aliquots of MNV@DHA were placed in a dialysis tube with a MWCO of 12 000–14 000, and transfer into 20 mL of corresponding buffers, respectively. At the desired time intervals, the release medium (5.0 mL) was taken out from each group and replenished with an equal volume of fresh medium. The DHA in the release medium was determined by HPLC according to a standard curve (Ultramate 3000, Thermo Fisher, USA). Release experiments were conducted in triplicate, and the results are presented as the average ± standard deviation.

In vitro cellular uptake assays

The cellular uptake behaviors of MNV@DHA were evaluated on both of RAW 264.7 cells and H22 cells. Briefly, cells were seeded into a 24-well plate (1×10^5 cells/well) and allowed it to grow for 12 h. Then, DiR-labelled MNV@DHA were added to cells and incubated for different time. After incubation, the culture medium was removed and the cells were washed twice with PBS. The cells were fixed with 4% of paraformaldehyde at room temperature for 15 min. The cell nucleus was stained with 5 μg/mL of DAPI at 37 °C for 10 min. The slides were examined under inverted fluorescence microscope and analyzed using the ImageJ software. The cellular uptake of nanovesicles was further quantified by flow cytometry. Briefly, both of RAW264.7 and H22 cells were cultured in a 24-well plate (2×10^5 cells/well) overnight followed by the treatments as mentioned above. The culture medium was discarded and the cells were prepared as suspensions, washed twice with PBS, re-suspended in PBS and analyzed by flow cytometry.

Oil Red O staining

The common and acid-adapted H22 cells (pH6.5) were utilized to analyze the accumulation of DHA under different pH conditions, respectively. Briefly, both the cells were seeded into 24-well plates and treated with different concentrations of DHA or MNV@DHA under different pH conditions for 12 h. After that, cells were washed twice with PBS and fixed in 4% of paraformaldehyde for 15 min. The cells were subsequently rinsed with 60% isopropanol. Oil Red O was then added and incubated for 30 min. Then, the cells were washed with 60% of isopropanol to eliminate unbound dye. Hematoxylin was used to counterstain and bright-field images were taken at 40 × magnification using

Olympus BX43. The staining was semi-quantitatively measured by reading the absorbance at 492 nm of re-dissolved Oil Red O in isopropanol.

ROS detection

To detect the ROS production at the intracellular condition, H22 cells were seeded into a 24-well plate (1×10^5 cells/well), cultured overnight and treated with MNV, DHA, and MNV@DHA, respectively, for 24 h. Then, the cells were incubated with the ROS probe (20 μM) for 20 min. After that, the cells were washed with PBS, fixed by 4% formaldehyde and stained with DAPI. The fluorescence images were captured under fluorescence microscopy. To quantify the fluorescence intensity of ROS, the cells were performed as above described methods and then finally suspended in PBS for flow cytometry analysis.

Determination of intracellular GSH levels

H22 cells were seeded into a 6-well plate and cultured for 12 h. The cells treated with MNV, DHA, and MNV@DHA, respectively, for 24 h. After that, the GSH levels were determined according to manufacturer's instructions (BC1175, Solarbio). The collected cells were resuspended and lysed with freeze thaw method (2–3 times) in liquid nitrogen. Then, the sample were performed with centrifugation (8000 ×g) for 10 min. The suspensions were measured as described in the protocol by a Multi-mode Reader from BioTek and calculated according to a standard curve.

Western blot assay

H22 cells were incubated in 6-well plates at a density of 5×10^5 cells per well for 12 h. The cells were treated with PBS, MNV, DHA and MNV@DHA, respectively for 24 h. After that, the cells were collected and treated with NP-40 buffer and then the protein was harvested and separated by SDS-PAGE. After being transferred to a polyvinylidene difluoride membrane (Roche, USA), the primary antibodies (1: 1000) were used to detect the target proteins followed by HRP-conjugated secondary antibody and the ECL reagent kit treatment (Tanon, China). The images were collected using CLINX ChemiScope 6100.

CCK8 assay of cell viability

The cell viabilities of H22 cells with different treatments were evaluated by CCK8 assay (CA1210, Solarbio). Briefly, H22 cells were cultured in 96-well plates at a density of 1×10^4 cells for 12 h and then followed with different treatment for 48 h. Then a standard CCK-8 assay was used to determine the cell viability. The experiments were performed independently for three times.

Propidium iodide (PI) staining assay

The cell death of H22 cells was determined by PI staining assay and analyzed by flow cytometry. Briefly, H22 cells were cultured in 24-well plates at a density of 2×10^5 cells per well for 12 h. After that, the cells were pretreated with or without ferrostatin-1 (0.13 μg/mL) followed with different treatments for 48 h. Then, the cells were collected, stained with PI (5 μg/mL) for 15 min and proceed immediately with flow cytometry.

Fluorescence analysis

The expression of CD86 or CD206 was examined by fluorescence microscope and flow cytometry. For the expression of CD86 on RAW 264.7 cells, the cells were incubated with different treatment for 48 h and then the culture medium was removed and the cells were washed twice with PBS. After that, the cells were stained with Cy5.5-labelled CD86 antibodies for 30 min at 4 °C followed by three times of washing with PBS. Then, the cells were fixed with 4% of paraformaldehyde at room temperature for 15 min. The cell nucleus was stained with 5 μg/mL DAPI at 37 °C for 10 min. The slides were examined under inverted fluorescence microscope and analyzed using the ImageJ software. The expression of CD86 was further quantified by flow cytometry. Briefly, RAW264.7 were cultured in a 24-well plate (2×10^5 cells/well) overnight followed by the treatments as mentioned above. The culture medium was discarded and the cells were prepared as suspensions, stained with CD86 antibodies, washed twice with PBS, re-suspended in PBS and analyzed by flow cytometry. For CD206 expression on M2 macrophages, RAW 264.7 were pre-stimulated with IL-4 (20 ng/mL) for 48 h and then incubated with different formulations for 48 h. The examination was performed by fluorescence microscope and flow cytometry as mentioned above.

In vivo biodistribution

In vivo biodistribution of MNV@DHA was demonstrated using the C57BL/6 mice bearing orthotopic H22-Luc cell tumor. C57BL/6 female mice (6 weeks old) were purchased from Hangzhou Ziyuan Laboratory Animal Science and Technology Co., Ltd. (Hangzhou, China). All animal experiments were carried out in compliance with the Animal Management Rules (Ministry of Health, People's Republic of China) and the guidance for Care and Use of Laboratory Animals (China Pharmaceutical University). The mouse liver cancer model was established by orthotopic injection of H22-Luc cells (2.0×10^4 per mouse). After 5 days, the growth of the tumor was determined by IVIS system, and the tumor bearing mice were randomly grouped and injected with a single dose of DiR-labeled RNV@DHA and MNV@DHA (DHA: 30 mg/kg) in 100 μL of PBS via tail vein. At designated time intervals (1, 2, 3, 5, 8, 24 h) post-injection, the fluorescence images were acquired. At the end of experiments, the main organs were dissociated after euthanasia for ex vivo fluorescence imaging. The fluorescence images were scanned using a near-infrared fluorescence imaging system (IVIS® Lumina™, USA), and the images were acquired and analyzed using the Living Image software (PerkinElmer, USA).

Evaluation of the antitumor effect and tumor-infiltrating lymphocytes

The mouse liver cancer model was established by orthotopic injection of H22-Luc cells (2.0×10^4 per mouse). After five days, the growth of the tumor was determined by IVIS system, and the tumor-bearing C57BL/6 mice were randomly divided into four groups ($n = 5$): PBS, MNV, DHA and MNV@DHA (DHA: 30 mg/kg). Each group of tumor-bearing mice was injected with 100 μL of the formulations through the tail vein. The administrations were performed on day 0, 3, 7 and 10. During the treatment period, the bodyweight of the mice was measured and recorded every other day. The bioluminescence intensity of the tumor-bearing mice was imaged and calculated using an IVIS device after the injection of D-luciferin potassium salt to monitor the tumor growth. At

the end of experiments, three of tumor-bearing mice from each group were sacrificed. The liver tissues were harvested and processed for hematoxylin–eosin (H&E) staining and immunohistochemistry (IHC) of Ki67 and GPX4 to evaluate the antitumor effect. The major organs were also stained by H&E for systemic toxicity analysis. In a paralleled experiment, the mice were divided into four groups ($n=4$) and treated with different formulations as mentioned above. At the end of different treatments, the H22- tumor-bearing mice were performed with euthanasia and then the orthotopic tumor tissues were separated to cut into smaller pieces and digested in 1640 medium with 0.5 mg/mL of type IV collagenase for 1 h at 37 °C. The digested tissues were gently meshed through a 70 μm cell strainer and then stained with various fluorophore-conjugated antibodies for 30 min in dark condition. The immune cells were stained with anti-CD45–FITC (BD Pharmingen™, Lot: 553079), anti-CD11b-Percp-Cy5.5 (BD Pharmingen™, Lot: 550993), anti-F4/80-BV510 (BD OptiBuild™,Lot:743280), anti-CD86-BV421(BD Horizon™, Lot:564198), anti-CD206-APC (eBioscience, LOT: 17–2061-82), anti-CD3-Percp-cy5.5 (BD Pharmingen™, Lot: 551163), anti-CD8-APC (BD Pharmingen™, Lot: 553035) antibodies according to the manufacture's protocols. After washing, the cells were used for flow cytometry analysis (Beckman, Cytoflex FCM, USA). The data were processed by FlowJo software.

Statistical analysis

Quantitative data were presented as the mean ± standard error, with $^{*}p<0.05$, $^{**}p<0.01$ and $^{***}p<0.001$ indicating statistical significance. One-way analysis of variance (ANOVA) was adopted to compare more than two groups and the two-tailed Student's t-test for between-group comparison.

Results and discussion

Preparation and characterization of MNV@DHA

The exosome-mimetic MNV loading with DHA was prepared by serially extruding LPS and IFN-γ-treated RAW 264.7 cells (M1 macrophage) with different pore size of polycarbonate membranes (Scheme 1). The expression of CD86 was confirmed by flow cytometry serving as the marker of M1 macrophages (Additional file 1: Fig. S1). Furthermore, the activated markers of M1 macrophages were also detected with high expression in MNV such as iNOS and IL-6 indicating that MNV might inherit the immune activation of M1 macrophages (Additional file 1: Fig. S2). The size distribution and morphology of the nanovesicles were examined by DLS and TEM. As shown in Fig. 1A, B, the mean diameter of MNV and MNV@DHA was 136.5 and 188.8 nm, respectively. Moreover, the zeta potential determination revealed that MNV@DHA was characterized with negative potential, which could be advantaged to the long circulation of the nanovesicles (Fig. 1C). The stability of MNV@DHA in PBS and 10% of serum was measured by DLS (Fig. 1D). The results showed no significant alternation of hydrodynamic diameter in PBS or serum for 72 h. The components of MNV were evaluated by Coomassie blue staining indicating that the protein bands of MNV were less than M1 macrophages. However, the loading of DHA into MNV exhibited no influence on the protein bands of MNV (Fig. 1E). The drug loading efficacy of DHA could reach to 95.4% at a feed ratio of 5% (weight %) determined by HPLC (Additional file 1: Table S1). Additionally, the

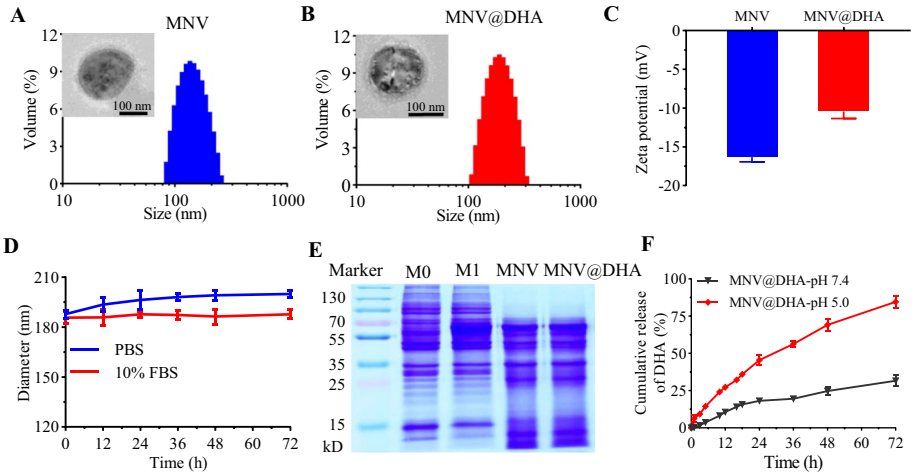

Fig. 1 Characterization of MNV@DHA. **A**–**B** The diameter and morphology of MNV (**A**) and MNV@DHA (B). **C** Zeta-potential of MNV and MNV@DHA. **D** The diameter alteration of MNV@DHA at different conditions for 72 h. **E** Coomassie blue staining for the protein bands of different formulations separated by SDS-PAGE. M0 and M1 indicated the protein extracted from M0 and M1 macrophages, respectively. **F** The cumulative release of DHA at different pH conditions determined by HPLC

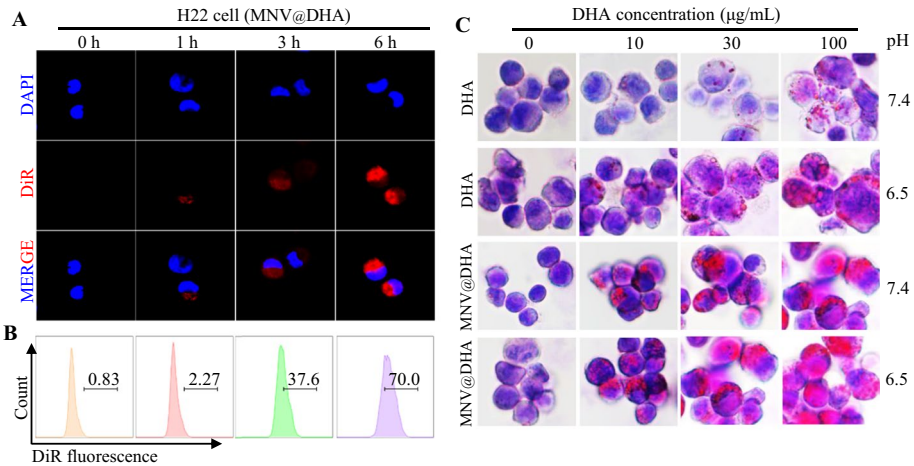

Fig. 2 Cell endocytosis and DHA accumulation in H22 cells. **A**–**B** DiR-stained MNV@DHA (10 μg/mL of DHA) was incubated with H22 cells for indicated time and examined by fluorescence microscope (**A**) and flow cytometry (**B**). **C** Different concentrations of DHA or MNV@DHA were incubated with normal or acid-adapted H22 cells for 24 h at different pH conditions and then stained with Oil Red O

cumulative release of DHA at different pH conditions was examined. The results demonstrated that acidic pH could significantly accelerated the in vitro release of DHA from MNV that more than 84.3% of DHA was released in 72 h of pH 5.0, and only 31.6% of DHA was released at pH 7.4.

Acidic pH condition promotes the accumulation of DHA in tumor cells

DHA could be successfully loaded into MNV, which might be advantaged to the cellular uptake of DHA. Firstly, the fluorescent dye of DiR was utilized to stain MNV for endocytosis study. As shown in Fig. 2A, B, DiR-stained MNV could be significantly endocytosed

by H22 cells indicated by the increased fluorescence intensity dependent on the incubation time (Additional file 1: Fig. S3). Accordingly, the uptake and accumulation of DHA in H22 cells were studied under different pH conditions. As shown in Fig. 2C and Additional file 1: Fig. S4, significantly more DHA were accumulated in H22 cells after being loaded by MNV compared to free DHA. More importantly, acid-adapted cancer cells (pH6.5) simulating the microenvironment of tumor tissues could increase more DHA accumulation compared to that of normal H22 cells at neutral condition (pH7.4). These results indicated that acidic tumor microenvironment was beneficial to the tumor cells to capture more DHA, which could be further enhanced when DHA was loaded into MNV. Therefore, MNV@DHA might play an important role in the antitumor therapy.

MNV@DHA induce cell death via ferroptosis

DHA had been reported to induce ferroptosis of tumor cells in previous studies (Dierge et al. 2021). Accordingly, ROS accumulation and GSH consumption, the important characteristics of ferroptosis (Wei et al. 2022), were examined on H22 cells with different treatments. As show in Fig. 3A, DHA could significantly induce the release of ROS while PBS treatment exhibited no obvious fluorescence. Instead, MNV@DHA could induce more ROS generation contributed the enhanced cellular uptake and accumulation of DHA since MNV did not mediate significant ROS release. The consumption of GSH exhibited the paralleled effect that MNV@DHA mediated the maximum reduction of GSH (Fig. 3B). The cellular ferroptosis marker of glutathione-dependent peroxidase 4 (GPX4) serving as a lipid repair enzyme could be deactivated during ferroptosis (Li P. et al. 2021a). Accordingly, the protein level of GPX4 was examined exhibiting that DHA could significantly decrease GPX4 expression and combining MNV with DHA could further aggravate the reduction of GPX4. A similar decreased trend was observed for

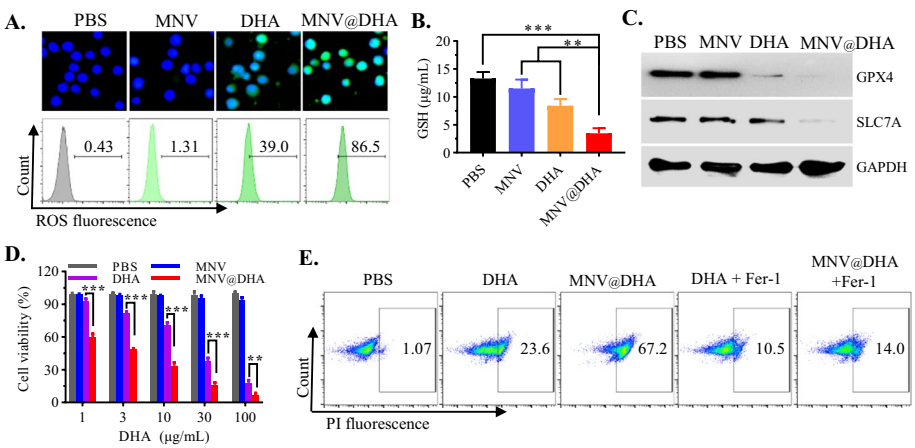

Fig. 3 Enhanced ferroptosis induced by MNV@DHA. **A** H22 cells were incubated different formulations (10 μg/mL of DHA) for 24 h followed by examining with fluorescence microscope (upper panel) and flow cytometry (lower panel). **B** H22 cells were treated with different formulations (10 μg/mL of DHA) for 24 h and then the cells were lysed for GSH determination. **C** H22 cells were performed with different treatments (10 μg/mL of DHA) for 24 h and then the protein was extracted for western blot assay. **D** H22 cells were incubated with different concentrations of the indicated formulations for 48 h and then cells were performed with CCK8 assay. **E** H22 cells were pretreated with or without ferrostatin-1 (Fer-1, 0.13 μg/mL) for 30 min and then treated with different formulations (10 μg/mL of DHA) for 48 h followed by PI staining for flow cytometric analysis

the cystine/glutamate transporter SLC7A11 (SLC7A), which was critical to support cellular GSH biosynthesis (Fig. 3C). Therefore, the cell viability of H22 cells was evaluated by CCK8 assay and the results demonstrated that DHA could decrease cell viability in a concentration-depending manner. Although free MNV did not exhibit activity against cell viability, the combination of MNV and DHA exhibited the strongest in vitro antitumor activity (Fig. 3D). The pattern of cell death was confirmed by using a ferroptosis inhibitor. As shown in Fig. 3E, the inhibitor could significantly reverse the cell death induced by DHA or MNV@DHA indicated by the change of PI-positive cells. Furthermore, the antitumor activity of MNV@DHA was also evaluated on human HCC of HepG2 and SMMC-7721. The results demonstrated the the antitumor activity of MNV@DHA was consistent with previous results, and MNV@DHA showed stronger activity against human HCC cells than that of murine H22 cells (Additional file 1: Fig. S5).

In vitro polarization of macrophages induced by MNV@DHA

M1 macrophage-derived exosomes had been reported to be able to induce the polarization of M1 macrophage, which played an important role in the immune activation of TIME. Therefore, cellular uptake behaviors of RAW264.7 for MNV@DHA was firstly examined. As shown in Fig. 4A, B and S6, the DiR-stained MNV@DHA could be endocytosed by macrophages indicated by the increased fluorescence inside the cells and the fluorescence could be detected in about 90.1% of the cells after 6 h of the incubation. The polarization of M1 macrophage was examined by detecting the expression of CD86. As shown in Fig. 4C, D, the fluorescence could be detected in both of MNV and MNV@DHA treatment groups demonstrating that MNV could induce the polarization of M1 macrophage. It was interesting that MNV also could repolarize M2 macrophage

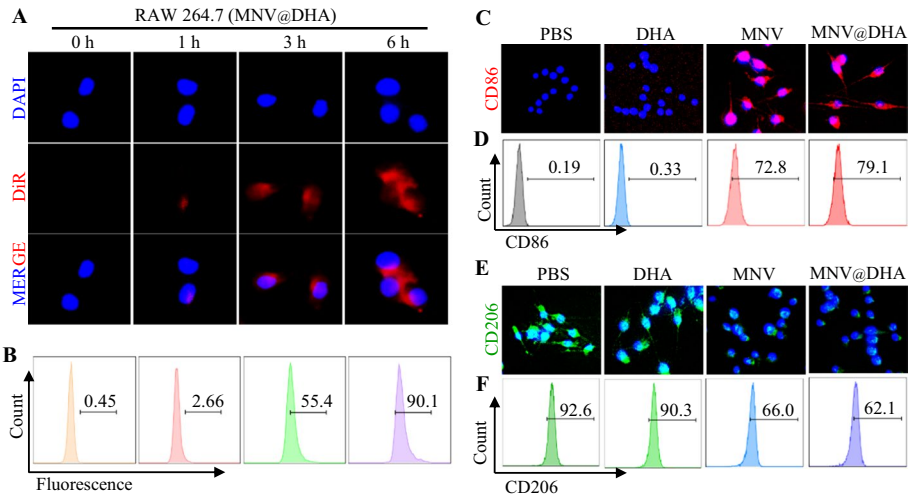

Fig. 4 In vitro immune-regulated effect on macrophage polarization. **A**–**B** Cell endocytosis of MNV@DHA in RAW 264.7 cells. DiR-stained MNV@DHA (10 μg/mL of DHA) was incubated within RAW 264.7 cells for indicated time and examined by fluorescence microscope (**A**) and flow cytometry (**B**). **C**–**D** RAW 264.7 cells (M0) were incubated with different formulations (10 μg/mL of DHA) for 48 h and then stained with anti-CD86 for fluorescence microscope (**C**) and flow cytometric analysis (**D**). (**E**–**F**) RAW 264.7 cells were pretreated with IL-4 (20 ng/mL) for 48 h. The cells were rinsed with PBS for three times and then incubated with different formulations (10 μg/mL of DHA) for 48 h followed by staining with anti-CD206 for fluorescence microscope (**E**) and flow cytometric analysis (F)

indicated by the decreased expression of CD206 (Fig. 4E, F). These results demonstrated that MNV could mediate immune activation by regulating macrophages, which might be advantaged to in vivo antitumor activity of MNV@DHA.

In vivo biodistribution of MNV@DHA

To explore the in vivo tumor target ability of MNV, the erythrocyte membrane derived nanovesicles (RNV) was utilized as a control to compare with MNV on a murine orthotopic hepatocellular carcinoma model. The H22-Luc tumor bearing mice were divided into two groups and intravenously injected with DiR-stained RNV@DHA and.

MNV@DHA, respectively. The fluorescence was examined at different time intervals. As shown in Fig. 5A, the fluorescence of both groups could rapidly accumulate at the liver in 1 h and the fluorescence gradually increased within 8 h of the examination. However, the fluorescence in ex vivo organs analysis demonstrated that more fluorescence was detected at orthotopic tumor tissues separated from MNV group, while RNV-treated mice exhibited no obviously specific distribution at the tumor site (Fig. 5B). The results indicated that MNV might be more likely to target tumor tissues than RNV contributed from M1-derived chemotaxis for inflammation.

In vivo antitumor performance of MNV@DHA

Since MNV could be accumulate at tumor tissues, the in vivo antitumor effect of DHA-loaded MNV was evaluated on H22-Luc tumor bearing mice. When the murine orthotopic liver cancer was successfully established, the tumor-bearing mice were divided into four groups and intravenously administrated with four times of PBS, MNV, DHA, and MNV@DHA, respectively, on day 0, 3, 7, and 10. The bioluminescence intensity was determined to monitor tumor growth. As shown in Fig. 6A, B and S7, MNV or DHA treatments only exhibited moderate antitumor effect in vivo compared to PBS group. However, it was worthy noticing that the combination of MNV and DHA exhibited stronger activity against tumor growth than other treatments. The antitumor effect of MNV@DHA was confirmed by excised liver tissues and the results indicated that the visible tumor tissues in MNV@DHA-treated liver were significantly smaller than other groups (Fig. 6C). Accordingly, the tumor progress was further examined by H&E staining and IHC for Ki67 revealing that the tumor cells

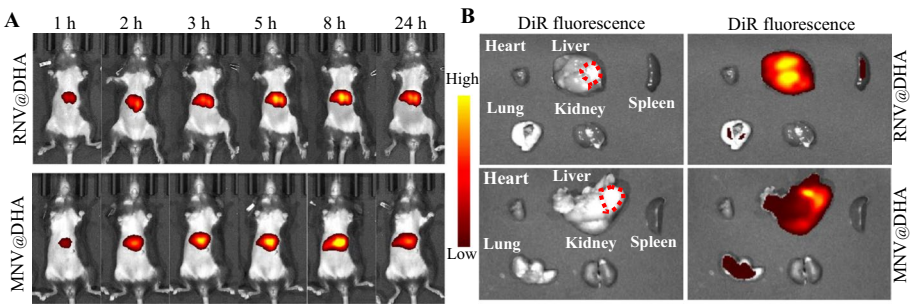

Fig. 5 In vivo fluorescence of DiR-stained RNV@DHA and MNV@DHA on a murine orthotopic H22-Luc tumor-bearing mice. **A** Real-time fluorescence images of H22-Luc tumor-bearing mice with 100 μL of different intravenous administrations (DHA: 30 mg/kg). **B** Representative ex vivo fluorescence images of tumors and other tissues of mice upon above treatments. The red circles highlight the regions of tumors

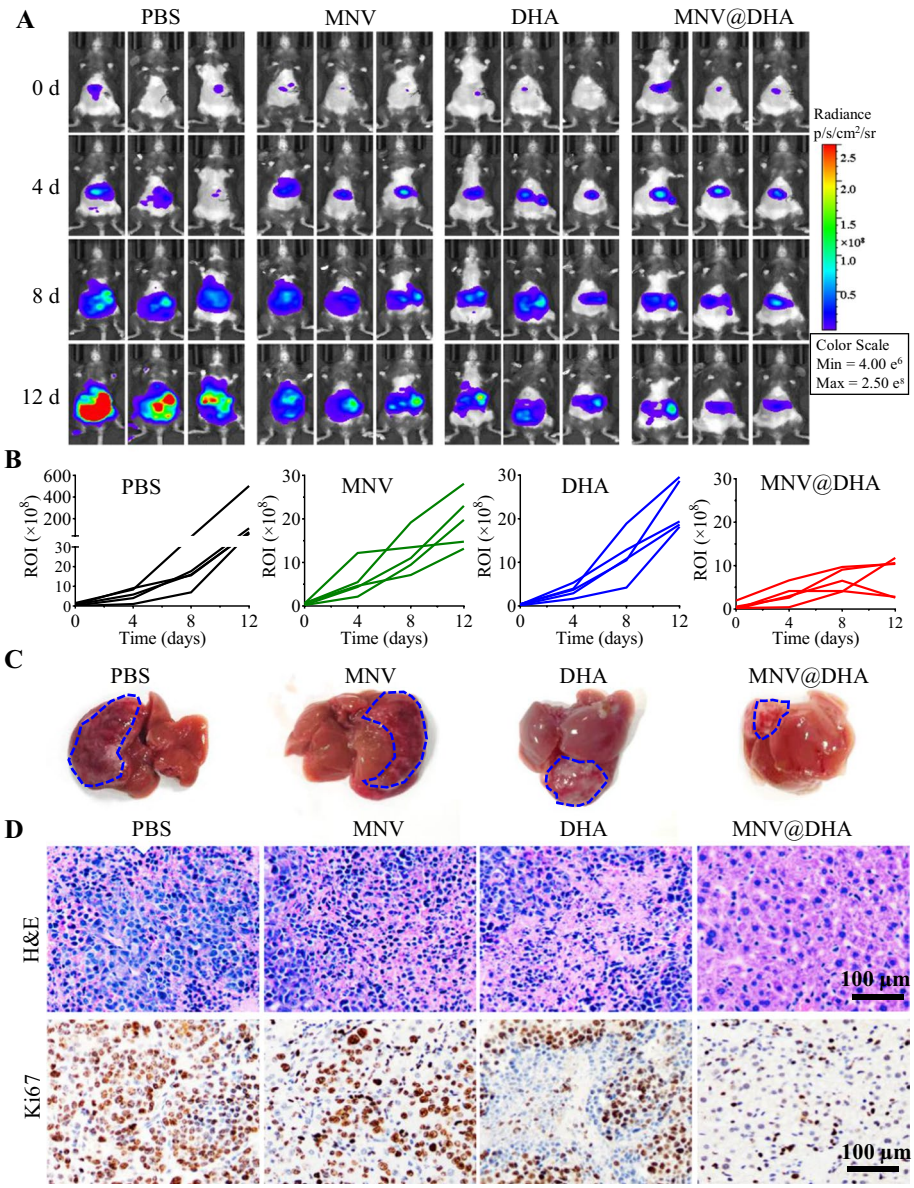

Fig. 6 In vivo antitumor evaluation of MNV@@DHA. **A**–**B** Represented in vivo bioluminescent images and ROI calculation at different time intervals to monitor tumor growth. **C** Represented liver tissues excised from euthanized mice. **D H** and **E** staining and IHC of Ki67 analysis of tumor tissues isolated from mice after 12 day of treatments

and Ki67-positive cells were significantly lessened in MNV@DHA group (Fig. 6D and Additional file 1: Fig. S8). Furthermore, the systemic toxicity of MNV@DHA was evaluated by determining the bodyweight change during the experimented period and H&E staining of major organs. The bodyweight of mice treated with MNV@DHA exhibited no bodyweight lost (Additional file 1: Fig. S9) and no appreciable damage was observed in major organs including the heart, spleen, lung and kidney at the end of experiments, indicating that the combined treatments had a good biocompatibility (Additional file 1: Fig. S10). Furthermore, the serum levels of alanine aminotransferase (ALT) and aspartate aminotransferase (AST) were determined to evaluate liver

function. The results demonstrated that there was no difference among groups indicating the safety of MNV@DHA (Additional file 1: Fig. S11).

In vivo immune performance

The combination of MNV and DHA exhibited the strongest antitumor activity, which might be contributed from ferroptosis and the activation of tumor immune microenvironments. Therefore, the GPX4 expression was examined in tumor tissues with different treatments. As shown in Fig. 7A and Additional file 1: S12, free DHA treatment could decrease the expression of GPX4 compared with PBS group. It was noticed that the expression of GPX4 was also reduced by MNV treatment, which might be contributed from the immune activation of TIME. Expectedly, MNV@DHA exhibited

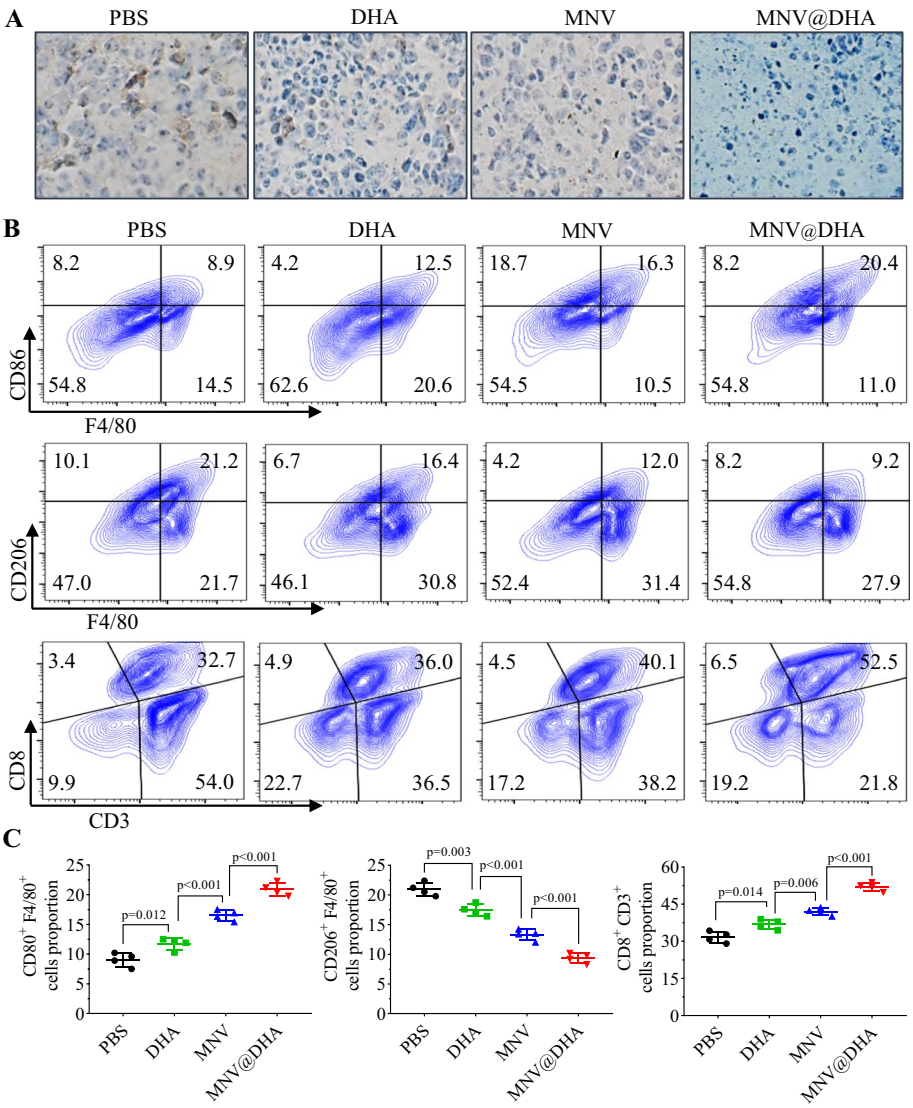

Fig. 7 Analysis of immune cell subsets from the tumor tissues with different treatments for 12 days. **A** Immunohistochemistry images of the expression of GPX4. (B-C) Flow cytometric analysis of M1 ($F4/80^+CD86^+$), M2 ($F4/80^+CD206^+$) and $CD8^+$T cells

stronger inhibition on GPX4 expression than free DHA, which might be explained from that MNV-mediated delivery of DHA could target tumor tissues for efficient ferroptosis induction and immune regulation. Accordingly, the tumor infiltrated lymphocytes were investigated to assess the immune response mediated by different treatment groups. As shown in Fig. 7B, C, the infiltration of M1 macrophages and $CD8^+$ T cells in the tumors was significantly increased in all the treatment groups compared with PBS group. However, MNV@DHA exhibited the strongest activation for the elevation of immune-activated cells. In contrast, the immune negative regulated cell of M2 macrophages were mostly decreased by the treatment of MNV@DHA indicating that combination of MNV and DHA could efficiently activate antitumor immune response.

Conclusion

To summarize, an engineering exosome-mimetic nanovesicle derived from M1 macrophages was prepared for DHA delivery. In vitro experiments demonstrated that MNV could efficiently loading with DHA and promote the accumulation of DHA in tumor cells facilitating the induction of ferroptosis. Furthermore, MNV@DHA exhibited prominent activities on the polarization of M1 macrophages and reprogramming of M2 macrophages. In a murine orthotopic hepatocellular carcinoma model, MNV@DHA could target tumor tissues, induce ferroptosis, and activate the immune microenvironments exhibiting strong in vivo antitumor activity. Overall, the characteristic of positive feedback regulation between ferroptosis and immune activation endowed MNV@DHA with tremendous potential for complementing pharmacological approaches for cancer management.

Supplementary Information

The online version contains supplementary material available at https://doi.org/10.1186/s12645-023-00166-x.

Additional file 1: Figure S1. The RAW 264.7 cells were incubated with 100 ng/mL of LPS and 50 ng/nL of IFN-γ for 24 h and then stained with anti-CD86-BV421 antibodies followed by flow cytometric analysis. **Figure S2.** Western blot assay for M_0NV (engineering M0-derived Nanovesicles) and MNV. **Figure S3.** Mean fluorescence intensity of H22 cells incubated with DiR-stained MNV@DHA for indicated time and determined by flow cytometry. **Figure S4.** Semi-quantitative measurement of Oil Red O staining by extracting the dye with isopropanol and reading the absorbance at 492 nm. **Figure S5.** CCK8 assay for HepG2 cells (**A**) and SMMC-7721 cells. The cells were incubated with different concentrations of the indicated formulations for 48 h and then the cells were performed with CCK8 assay. **Figure S6.** Mean fluorescence intensity of RAW 264.7 cells incubated with DiR-stained MNV@DHA for indicated time and determined by flow cytometry. **Figure S7.** The average ROI value for tumor growth. **Figure S8.** Semi-quantification of the Ki67 expression. **Figure S9.** Bodyweight variation of the mice with different treatments. **Figure S10.** H and E staining of the major organs excised from euthanized mice. **Figure S11.** The serum level of alanine aminotransferase (ALT) and aspartate aminotransferase (AST) from different groups. **Figure S12.** Semi-quantification of the GPX4 expression. **Table S1.** Drug loading efficacy (DLE) determined by HPLC with different drug loading contents (DLC).

Acknowledgements

This work was supported by grants from General project of Jiangsu Commission of Health (No. M2021110) and Taizhou Science and Technology Support Plan (Social Development, No. TN202106).

Author contributions

MM. and XZ performed the cell and animal experiments, analyzed the data, and wrote the manuscript. QL and JJH provided a series of experimental instructions and performed cell experiments. YC. and HSQ provided a series of experimental instructions on animal studies. YLY and XH designed, supervised, and wrote the manuscript. All the authors approved the final version of the manuscript.

Availability of data and materials

The data that support the findings of this study are available from the corresponding author upon reasonable request.

Declarations

Ethics approval and consent to participate
All animal experiments were carried out in compliance with the Animal Management Rules (Ministry of Health, People's Republic of China) and the guidance for Care and Use of Laboratory Animals (China Pharmaceutical University) and approved by the institutional research ethics committee of China Pharmaceutical University.

Consent for publication
All authors approve the manuscript and consent for the submission and publication.

Competing interests
The authors declare that they have no known competing financial interests or personal relationships that could have appeared to influence the work reported in this paper.

Received: 4 November 2022 Accepted: 15 February 2023
Published online: 07 March 2023

References

Chen X, Kang R, Kroemer G, Tang D (2021) Broadening horizons: the role of ferroptosis in cancer. Nat Rev Clin Oncol 18:280–296
Cheng L, Wang Y, Huang L (2017) Exosomes from M1-polarized macrophages potentiate the cancer vaccine by creating a pro-inflammatory microenvironment in the lymph node. Mol Ther 25:1665–1675
Choo YW, Kang M, Kim HY, Han J, Kang S, Lee JR, Jeong GJ, Kwon SP, Song SY, Go S et al (2018) M1 macrophage-derived nanovesicles potentiate the anticancer efficacy of immune checkpoint inhibitors. ACS Nano 12:8977–8993
Colegio OR, Chu NQ, Szabo AL, Chu T, Rhebergen AM, Jairam V, Cyrus N, Brokowski CE, Eisenbarth SC, Phillips GM et al (2014) Functional polarization of tumour-associated macrophages by tumour-derived lactic acid. Nature 513:559–563
Conrad M, Pratt DA (2019) The chemical basis of ferroptosis. Nat Chem Biol 15:1137–1147
Dierge E, Debock E, Guilbaud C, Corbet C, Mignolet E, Mignard L, Bastien E, Dessy C, Larondelle Y, Feron O (2021) Peroxidation of n-3 and n-6 polyunsaturated fatty acids in the acidic tumor environment leads to ferroptosis-mediated anticancer effects. Cell Metab 33(1701–1715):e1705
Haschka D, Hoffmann A, Weiss G (2021) Iron in immune cell function and host defense. Semin Cell Dev Biol 115:27–36
Jang SC, Kim OY, Yoon CM, Choi DS, Roh TY, Park J, Nilsson J, Lotvall J, Kim YK, Gho YS (2013) Bioinspired exosome-mimetic nanovesicles for targeted delivery of chemotherapeutics to malignant tumors. ACS Nano 7:7698–7710
Jiang Q, Wang K, Zhang X, Ouyang B, Liu H, Pang Z, Yang W (2020) Platelet membrane-camouflaged magnetic nanoparticles for ferroptosis-enhanced cancer immunotherapy. Small 16:e2001704
Kepp O, Kroemer G (2022) Pro-ferroptotic fatty acid metabolism renders cancer cells immunogenic. Trends Cancer 8:785–787
Kim KS, Choi B, Choi H, Ko MJ, Kim DH, Kim DH (2022) Enhanced natural killer cell anti-tumor activity with nanoparticles mediated ferroptosis and potential therapeutic application in prostate cancer. J Nanobiotechnology 20:428
Komai K, Shichita T, Ito M, Kanamori M, Chikuma S, Yoshimura A (2017) Role of scavenger receptors as damage-associated molecular pattern receptors in Toll-like receptor activation. Int Immunol 29:59–70
Li X, Liu R, Su X, Pan Y, Han X, Shao C, Shi Y (2019) Harnessing tumor-associated macrophages as aids for cancer immunotherapy. Mol Cancer 18:177
Li P, Gao MQ, Hu ZJ, Xu T, Chen JR, Ma YX, Li SW, Gu YQ (2021a) Synergistic ferroptosis and macrophage re-polarization using engineering exosome-mimic M1 nanovesicles for cancer metastasis suppression. Chem Eng J 409:128217
Li P, Jiang M, Li K, Li H, Zhou Y, Xiao X, Xu Y, Krishfield S, Lipsky PE, Tsokos GC, Zhang X (2021b) Glutathione peroxidase 4-regulated neutrophil ferroptosis induces systemic autoimmunity. Nat Immunol 22:1107–1117
Li Q, Yuan M, Jiao X, Huang Y, Li J, Li D, Ji M, Wang G (2021c) M1 macrophage-derived nanovesicles repolarize m2 macrophages for inhibiting the development of endometriosis. Front Immunol 12:707784
Liao P, Wang W, Wang W, Kryczek I, Li X, Bian Y, Sell A, Wei S, Grove S, Johnson JK et al (2022) CD8(+) T cells and fatty acids orchestrate tumor ferroptosis and immunity via ACSL4. Cancer Cell 40(365–378):e366
Luo X, Gong HB, Gao HY, Wu YP, Sun WY, Li ZQ, Wang G, Liu B, Liang L, Kurihara H et al (2021) Oxygenated phosphatidylethanolamine navigates phagocytosis of ferroptotic cells by interacting with TLR2. Cell Death Differ 28:1971–1989
Mantovani A, Marchesi F, Malesci A, Laghi L, Allavena P (2017) Tumour-associated macrophages as treatment targets in oncology. Nat Rev Clin Oncol 14:399–416
Molinaro R, Corbo C, Martinez JO, Taraballi F, Evangelopoulos M, Minardi S, Yazdi IK, Zhao P, De Rosa E, Sherman MB et al (2016) Biomimetic proteolipid vesicles for targeting inflamed tissues. Nat Mater 15:1037–1046
Nie W, Wu G, Zhang J, Huang LL, Ding J, Jiang A, Zhang Y, Liu Y, Li J, Pu K, Xie HY (2020) Responsive exosome nano-bioconjugates for synergistic cancer therapy. Angew Chem Int Ed Engl 59:2018–2022
Ou W, Mulik RS, Anwar A, McDonald JG, He X, Corbin IR (2017) Low-density lipoprotein docosahexaenoic acid nanoparticles induce ferroptotic cell death in hepatocellular carcinoma. Free Radic Biol Med 112:597–607
Pan Y, Yu Y, Wang X, Zhang T (2020) Tumor-associated macrophages in tumor immunity. Front Immunol 11:583084
Rodell CB, Arlauckas SP, Cuccarese MF, Garris CS, Li R, Ahmed MS, Kohler RH, Pittet MJ, Weissleder R (2018) TLR7/8-agonist-loaded nanoparticles promote the polarization of tumour-associated macrophages to enhance cancer immunotherapy. Nat Biomed Eng 2:578–588
Shan H, Dou W, Zhang Y, Qi M (2020) Targeted ferritin nanoparticle encapsulating CpG oligodeoxynucleotides induces tumor-associated macrophage M2 phenotype polarization into M1 phenotype and inhibits tumor growth. Nanoscale 12:22268–22280

Shen Z, Song J, Yung BC, Zhou Z, Wu A, Chen X (2018) Emerging strategies of cancer therapy based on ferroptosis. Adv Mater 30:e1704007
Wang W, Green M, Choi JE, Gijon M, Kennedy PD, Johnson JK, Liao P, Lang X, Kryczek I, Sell A et al (2019) CD8(+) T cells regulate tumour ferroptosis during cancer immunotherapy. Nature 569:270–274
Wei Y, Wang Z, Yang J, Xu R, Deng H, Ma S, Fang T, Zhang J, Shen Q (2022) Reactive oxygen species / photothermal therapy dual-triggered biomimetic gold nanocages nanoplatform for combination cancer therapy via ferroptosis and tumor-associated macrophage repolarization mechanism. J Colloid Interface Sci 606:1950–1965
Yang WS, SriRamaratnam R, Welsch ME, Shimada K, Skouta R, Viswanathan VS, Cheah JH, Clemons PA, Shamji AF, Clish CB et al (2014) Regulation of ferroptotic cancer cell death by GPX4. Cell 156:317–331
Yang Z, Xie J, Zhu J, Kang C, Chiang C, Wang X, Wang X, Kuang T, Chen F, Chen Z et al (2016) Functional exosome-mimic for delivery of siRNA to cancer: in vitro and in vivo evaluation. J Control Release 243:160–171
Zhang GL, Zhang L, Si YC, Li QD, Xiao JM, Wang B, Liang CZ, Wu ZY, Tian G (2020) Oxygen-enriched Fe3O4/Gd2O3 nanopeanuts for tumor-targeting MRI and ROS-triggered dual-modal cancer therapy through platinum (IV) prodrugs delivery. Chem Eng J. https://doi.org/10.1016/j.cej.2020.124269
Zhang HL, Hu BX, Li ZL, Du T, Shan JL, Ye ZP, Peng XD, Li X, Huang Y, Zhu XY et al (2022) PKCbetaII phosphorylates ACSL4 to amplify lipid peroxidation to induce ferroptosis. Nat Cell Biol 24:88–98
Zhao X, Di Q, Liu H, Quan J, Ling J, Zhao Z, Xiao Y, Wu H, Wu Z, Song W et al (2022) MEF2C promotes M1 macrophage polarization and Th1 responses. Cell Mol Immunol 19:540–553
Zhou Z, Xu B, Hu N, Guo Z, Bao W, Shao B, Yang W (2022) Targeting the macrophage-ferroptosis crosstalk: a novel insight into tumor immunotherapy. Front Biosci 27:203

Publisher's Note